Skeletal Radiol (2005) 34:245–259
DOI 10.1007/s00256-004-0872-9

REVIEW ARTICLE

Laura M. Fayad
Ihab R. Kamel
Satomi Kawamoto
David A. Bluemke
Frank J. Frassica
Elliot K. Fishman

Distinguishing stress fractures from pathologic fractures: a multimodality approach

Received: 5 May 2004
Revised: 7 September 2004
Accepted: 14 September 2004
Published online: 15 March 2005

L. M. Fayad (✉) · I. R. Kamel · S. Kawamoto · D. A. Bluemke · E. K. Fishman
The Russell H. Morgan Department of Radiology and Radiological Science, Johns Hopkins Medical Institutions, Baltimore, Maryland, USA
e-mail: lfayad1@jhmi.edu

F. J. Frassica
Orthopaedic Surgery, Johns Hopkins Medical Institutions, Baltimore, Maryland, USA

Abstract Whereas stress fractures occur in normal or metabolically weakened bones, pathologic fractures occur at the site of a bone tumor. Unfortunately, stress fractures may share imaging features with pathologic fractures on plain radiography, and therefore other modalities are commonly utilized to distinguish these entities. Additional cross-sectional imaging with CT or MRI as well as scintigraphy and PET scanning is often performed for further evaluation. For the detailed assessment of a fracture site, CT offers a high-resolution view of the bone cortex and periosteum which aids the diagnosis of a pathologic fracture. The character of underlying bone marrow patterns of destruction can also be ascertained along with evidence of a soft tissue mass. MRI, however, is a more sensitive technique for the detection of underlying bone marrow lesions at a fracture site. In addition, the surrounding soft tissues, including possible involvement of adjacent muscle, can be well evaluated with MRI. While bone scintigraphy and FDG-PET are not specific, they offer a whole-body screen for metastases in the case of a suspected malignant pathologic fracture. In this review, we present select examples of fractures that underscore imaging features that help distinguish stress fractures from pathologic fractures, since accurate differentiation of these entities is paramount.

Introduction

Although stress fractures are very common, they remain one of the most challenging problems in skeletal imaging. Stress fractures occur in normal or metabolically weakened bones, but, distinguishing these from pathologic fractures that occur at the site of bone tumors [1] can pose a significant diagnostic dilemma.

Stress fractures are classified into two groups: those that result from prolonged cyclical mechanical stresses on normal bone are referred to as *fatigue fractures*, while those that occur with physiologic stress on bones weakened by metabolic disease or radiation treatment are classified as *insufficiency fractures*. Fatigue fractures usually arise at select sites, specific for particular sports. For example, stress fractures of the tibia affect distance runners (Figs. 1, 2) [2, 3, 4], whereas stress fractures of the upper extremities are associated with baseball players [5]. However, almost any bone in the body can assume a stress fracture and it is useful to keep in mind that the incidence of fatigue fractures is increasing in the population, with runners now the most commonly affected group, accounting for 72% of stress fractures in a typical sports medicine practice [6].

Insufficiency fractures occur more commonly in the elderly and, in particular, in oncology patients. Many such patients have unsuspected fractures that are incidentally detected by computed tomography (CT) or magnetic resonance imaging (MRI) studies performed for other reasons. Also, skeletal scintigraphy and positron emission tomography (PET) scans ordered in oncology patients may demonstrate activity at the site of a stress fracture [7, 8, 9, 10, 11], and only careful attention to radiographic and cross-sectional imaging features will distinguish a

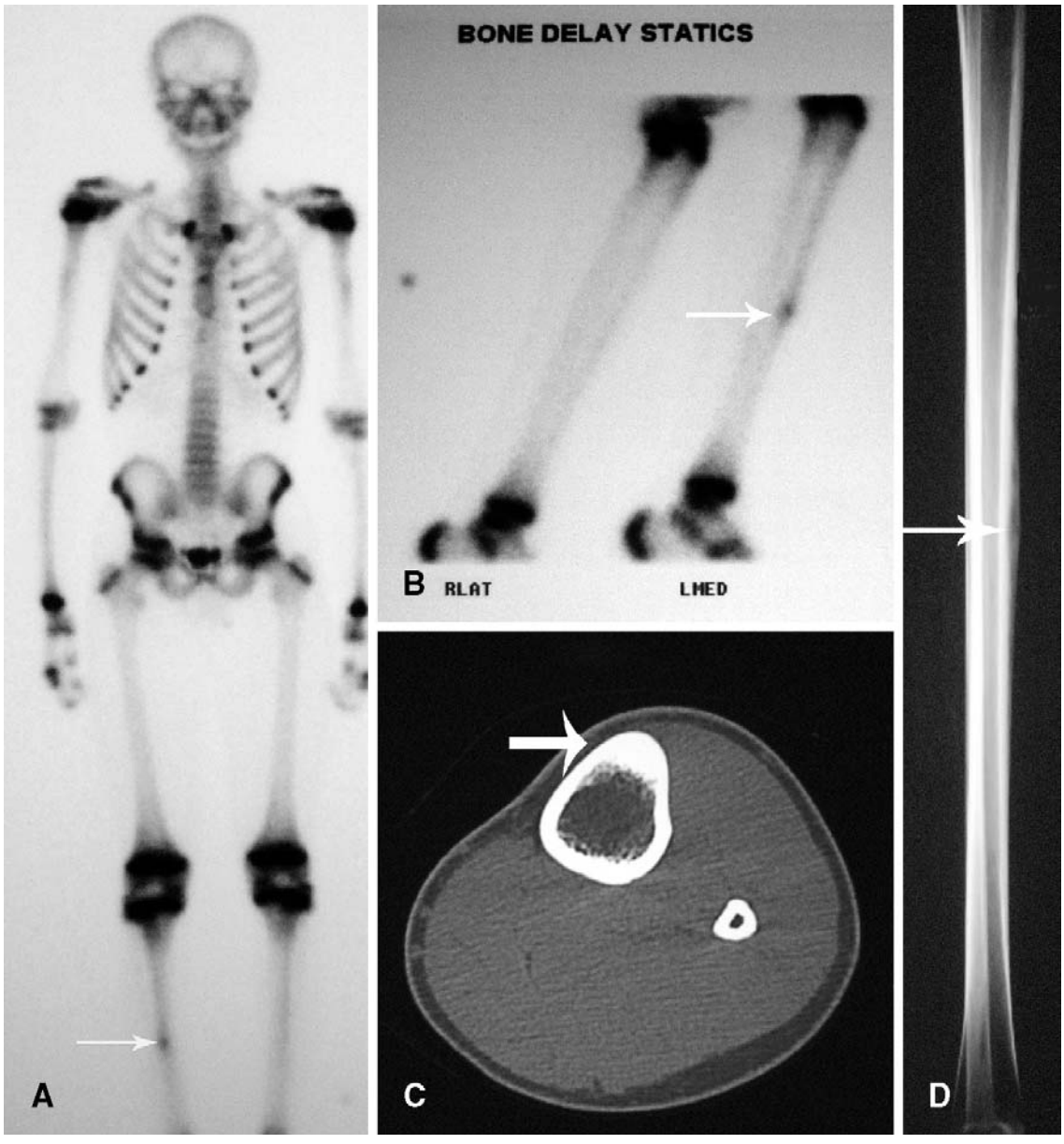

Fig. 1A—D A 15-year-old male runner with focal pain in the left mid-tibia who underwent CT imaging and bone scan. **A** Whole-body bone scan of the lower extremities in the posterior projection shows nonspecific focal uptake (*arrow*) in the left tibia. **B** Spot views of the lower extremities show nonspecific focal uptake (*arrow*) in the left tibia. **C** Axial high-resolution CT image performed with a 16-slice multidetector CT scanner shows subtle cortical thickening of the mid-diaphysis of the tibia (*arrow*). **D** Sagittal volume-rendered 3D CT image shows a horizontal stress fracture (*arrow*) in the mid tibial diaphysis. Because of the plane of the fracture, the fracture line was not displayed by axial images

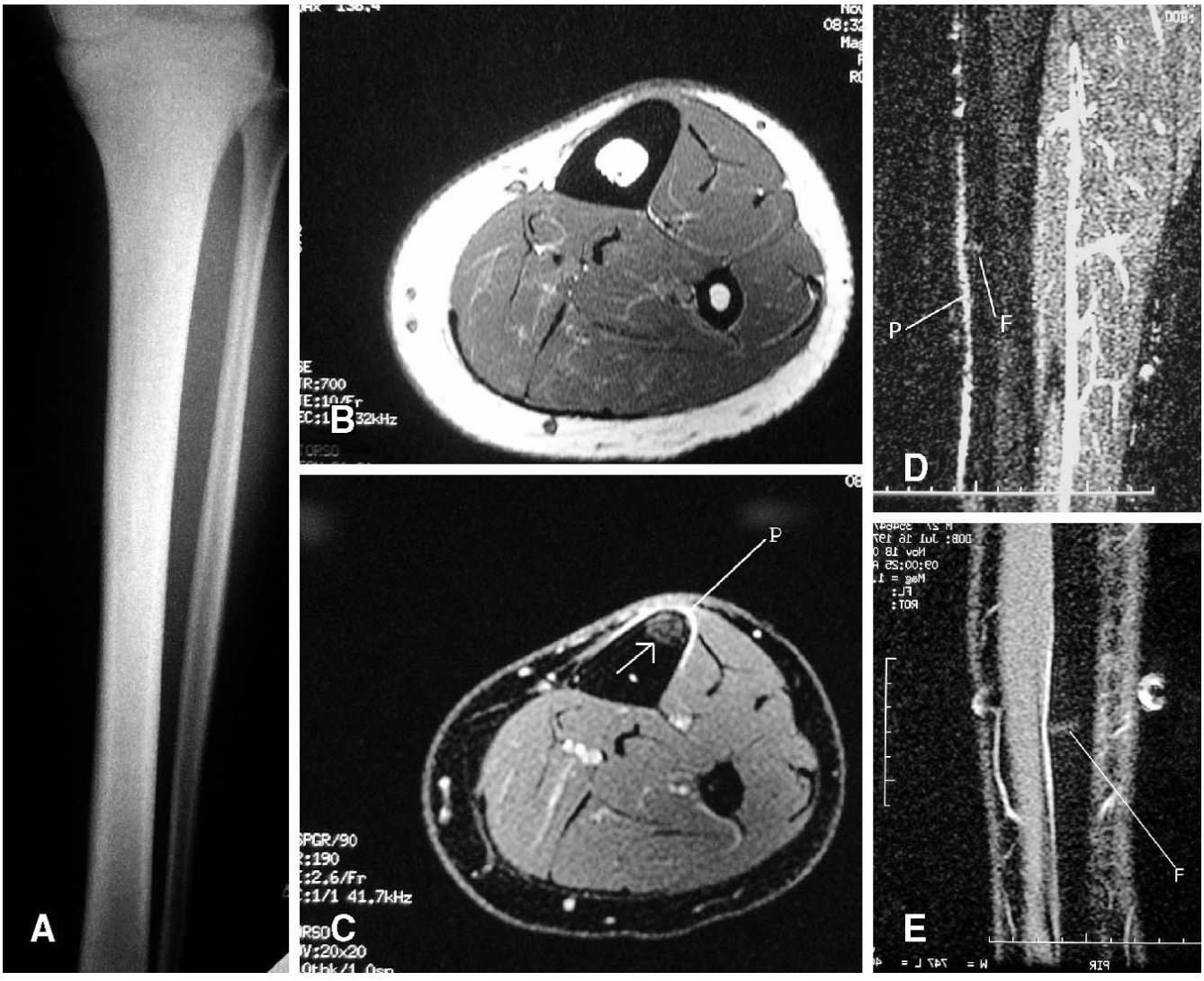

Fig. 2A—E An 18-year-old male competitive track runner with tibial pain. The importance of multiple imaging planes is again emphasized. **A** Radiograph of the tibia shows no abnormality. **B** Axial T1-weighted MR image (SE; TR 700, TE 10) at the level of the patient's pain shows no underlying bone marrow abnormality. **C** Axial post-contrast T1-weighted MR image (FSPGR; TR 190, TE 2.6, flip angle 90°) shows apparent nodular enhancement (*arrow*). Periostitis is marked (*P*). **D** Sagittal inversion recovery MR image (FSEIR; TR 3000, TE 30, TI 160) of the tibia shows a horizontal fracture line (*F*) and periostitis (*P*). **E** Sagittal post-contrast T1-weighted MR image (FSPGR; TR 190, TE 2.6, flip angle 90°) shows the fracture (*F*) more clearly. Apparent nodular enhancement on the axial image of **C** represents enhancement of the horizontal fracture line. Contrast is not needed for the evaluation of a fracture site, but enhancement of the fracture site augments detection of the fracture

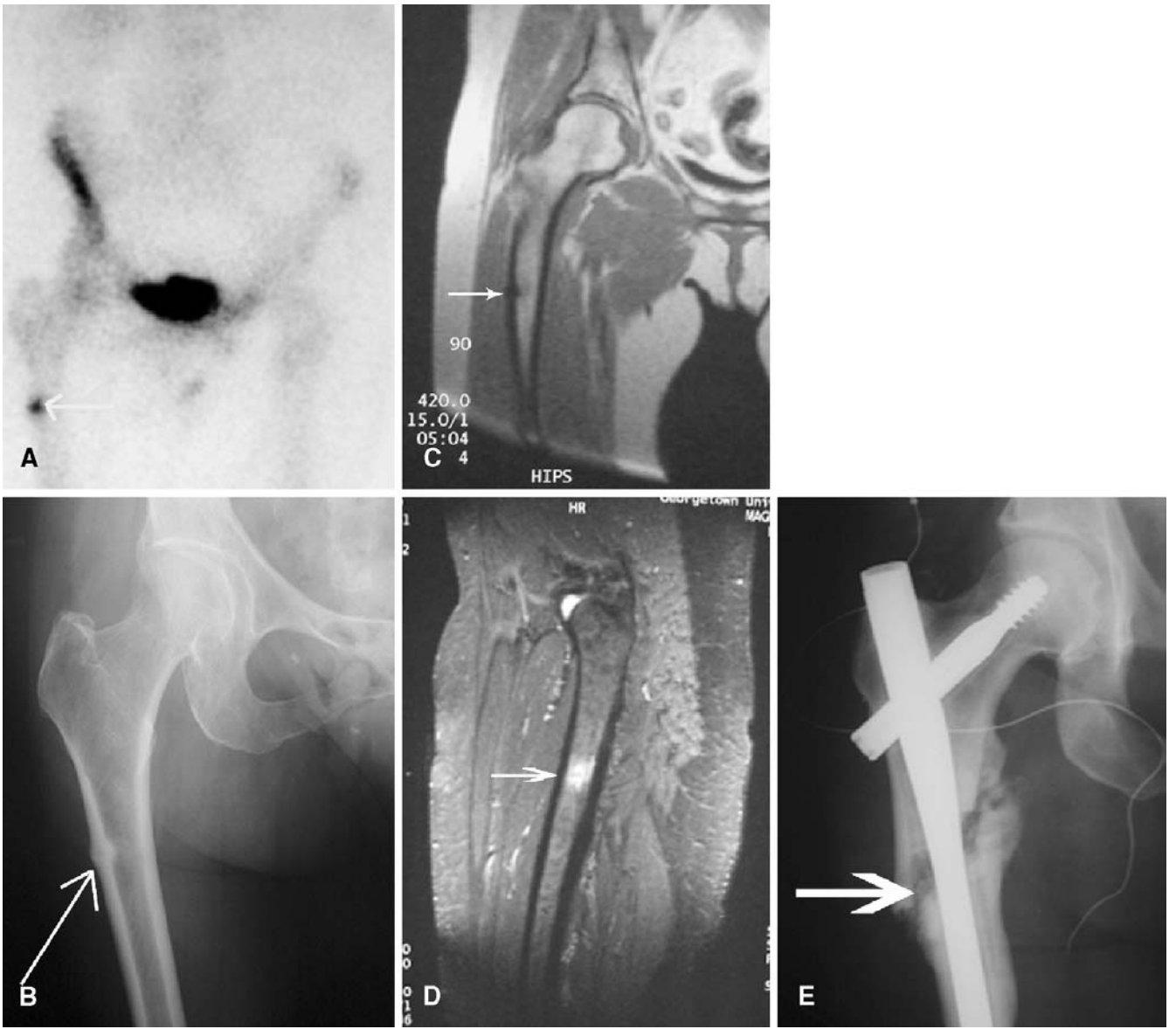

Fig. 3A—E A 59-year-old woman with history of breast cancer who underwent bone scanning, radiography and MRI for the evaluation of metastatic disease. Because her initial imaging was interpreted as consistent with a metastatic lesion, she underwent a course of radiation treatment to her femur. Subsequently, she was referred to our institution. **A** Bone scan shows focal uptake (*arrow*) in the right femur, a nonspecific finding which was reported as a metastatic lesion. **B** Radiograph of the right femur reveals focal cortical thickening (*arrow*) in the diaphysis. **C** Coronal T1-weighted MR image (SE; TR 420, TE 15) shows a stress fracture (*arrow*). Note the absence of an underlying bone marrow mass. Vague decreased T1 signal about the fracture line represents edema. **D** Coronal T2-weighted MR image (SE; TR 3500, TE 60) shows a stress fracture with surrounding bone marrow edema (*arrow*). This fracture was mistakenly reported as a suspicious lesion. **E** After therapy, the patient sustained a fall which resulted in a complete fracture of her right femur. A radiograph shows a cephalomedullary nail traversing the fracture (*arrow*). Biopsies of the area revealed no evidence of metastatic disease

Table 1 Most sensitive discriminating features between stress fractures and pathologic fractures

Modality	Stress fracture	Pathologic fracture
Radiograph	Endosteal thickening	Aggressive bone marrow pattern of destruction
	Benign periosteal reaction	Mineralized matrix
	Absence of any aggressive features	Endosteal scalloping
		Aggressive periosteal reaction
		Soft tissue mass
CT	Endosteal thickening	Aggressive bone marrow and cortical destruction
	Benign periosteal reaction	Mineralized matrix
	Absence of any aggressive features	Endosteal scalloping
		Aggressive periosteal reaction
		Soft tissue mass
MRI	Linear or band-like signal abnormality	Well-defined T1 bone marrow abnormality
	Surrounding bone marrow T2 abnormality (edema)	Endosteal scalloping
	Absence of or ill-defined T1 bone marrow abnormality	Massive muscle edema
		Soft tissue mass
Scintigraphy	Focal or linear uptake	Diffuse uptake
PET scan	Focal or linear uptake	Diffuse uptake

stress fracture from a metastatic lesion or pathologic fracture. Misdiagnosis of a stress fracture can have dire consequences, as illustrated in Fig. 3.

Therefore, while the clinical setting of a fracture is often helpful, the patient population in which stress and pathologic fractures can occur, overlaps. Hence, optimal evaluation of a fracture rests with the radiologist, who must detect the insidious underlying tumor in an otherwise healthy patient or, conversely, detect a stress fracture in an oncology patient (Figs. 1, 2, 3, 4, 5, 6, 7, 8, 9, 10, 11, 12). Table 1 summarizes the distinguishing features of stress and pathologic fractures with each imaging modality.

Plain radiograph evaluation

The first line of diagnosis is usually the conventional plain radiograph. However, the limitations of radiography are well recognized. The initial appearance of a fracture may be normal or nondiagnostic in the case of a stress fracture [12, 13, 14, 15,], and misinterpreted in the case of a pathologic fracture. Stress fracture appearance was originally described on radiographs with the classic features of a lucent fracture line associated with sclerosis, benign periosteal reaction and endosteal cortical thickening [16]. Stress fractures typically occur at specific locations in the body related to specific activities. Table 2 lists the typical stress fracture locations associated with various activities [16]. Nevertheless, features are influenced by location and time between injury and radiographic examination [17, 18], occasionally producing a deceptive radiographic appearance. For example, a relatively aggressive appearance due to exuberant osteolysis around a fracture site may confuse a stress fracture with a pathologic fracture [16]. The differential diagnosis at such a stage can also include a variety of malignancies including osteosarcoma and Ewing's sarcoma.

Table 2 Typical locations of stress fractures by activity (modified from [16])

Location of stress fracture	Activity
Ulna-coronoid	Pitching
Humerus-distal diaphysis	Throwing
Ribs	Carrying heavy objects
	Golf
Lower cervical spine	Clay shoveling
Lumbar spine (spondylolysis)	Lifting
	Ballet
Obturator ring	Bowling
	Gymnastics
Femur diaphysis and neck	Ballet
	Running
Fibula, distal	Running
Fibular, proximal	Jumping
Tibia	Running
Calcaneus	Jumping
Tarsal navicular	Marching/running
Metatarsal diaphysis	Marching

Similarly, the initial presentation of a pathologic fracture may be misinterpreted [19, 20, 21], with a missed opportunity for appropriate treatment. Again, location of the fracture plays a role in raising awareness of a potential pathologic fracture. Three locations are typically associated with pathologic fractures: the subtrochanteric femur, the junction of the humeral head and humeral metaphysis, and the spine [16]. However, in our experience, close to 10% of pathologic fractures are not confidently detected by the plain radiograph.

Thus, following an initial radiograph, advanced imaging techniques are often employed for further evalua-

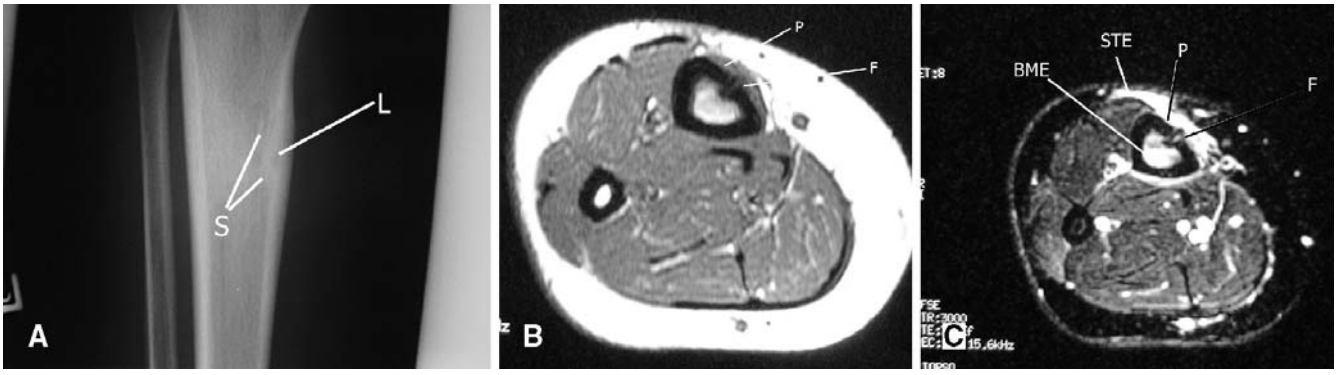

Fig. 4A—C A 25-year-old man with history of tibial pain and no definitive history of injury. Radiography was inconclusive and the patient subsequently underwent MRI. **A** Radiograph shows a focal lucency (*L*) surrounded by sclerosis (*S*). Differential diagnosis includes a stress fracture as well as other entities such as osteoid osteoma. **B** Axial T1-weighted MR image (SE; TR 400, TE 9) shows a fracture line (*F*) and periostitis (*P*). Bone marrow signal is relatively preserved with vague decreased signal representing edema. **C** Axial T2-weighted MR image (FSE; 3000, 75) shows a linear fracture line (*F*) with associated bone marrow edema (*BME*), periostitis (*P*) and soft tissue edema (*STE*). This fracture was followed to resolution

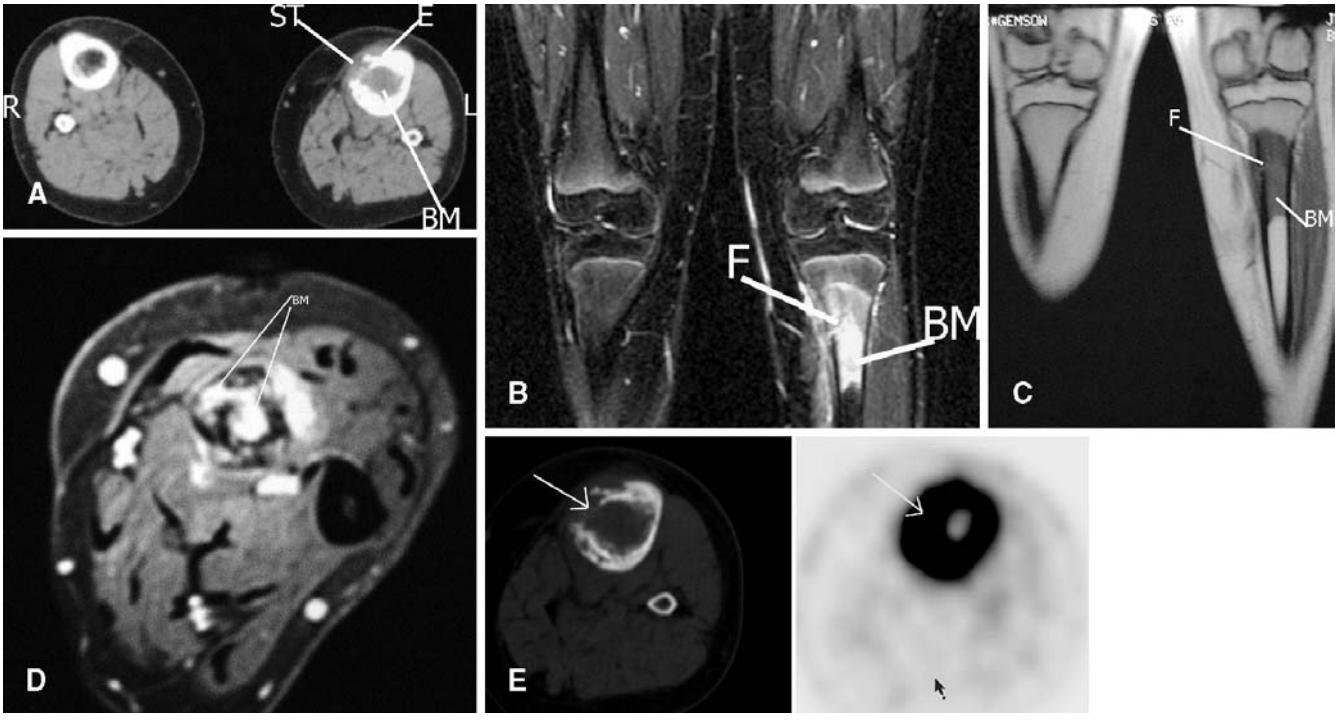

Fig. 5A—E A 12-year-old boy with a tibial fracture following a sports injury. **A** Axial CT image at the level of the fracture shows increased density in the medullary canal (*BM*) as well as cortical erosion (*E*) and a soft tissue prominence (*ST*). Compare the appearance of the abnormal left tibia (*L*) with the normal right tibia (*R*). **B** Coronal T2-weighted MR image (FSE; 3500, 65) shows a fracture line (*F*) with nonspecific surrounding increased bone marrow signal. **C** Coronal T1-weighted MR image (SE; 420, 12) shows a well-demarcated bone marrow signal abnormality in the tibia (*BM*) about the fracture line (*F*). Subsequent biopsy and excision revealed osteosarcoma. **D** Axial T1-weighted MR image (FSPGR; 200, 3.9, flip angle 80°) following intravenous contrast administration shows nodular enhancement in the bone marrow corresponding to tumor involvement (*T*). However, note that, in general, contrast is not necessary for the evaluation of pathologic fractures. **E** Axial FDG-PET scan at the level of the pathologic fracture showing intense uptake in the tumor (*arrow*). Corresponding CT image shows destruction of the cortex (*arrow*). Be aware that pathologic fractures are difficult to evaluate by PET as stress fractures may also demonstrate increased FDG uptake

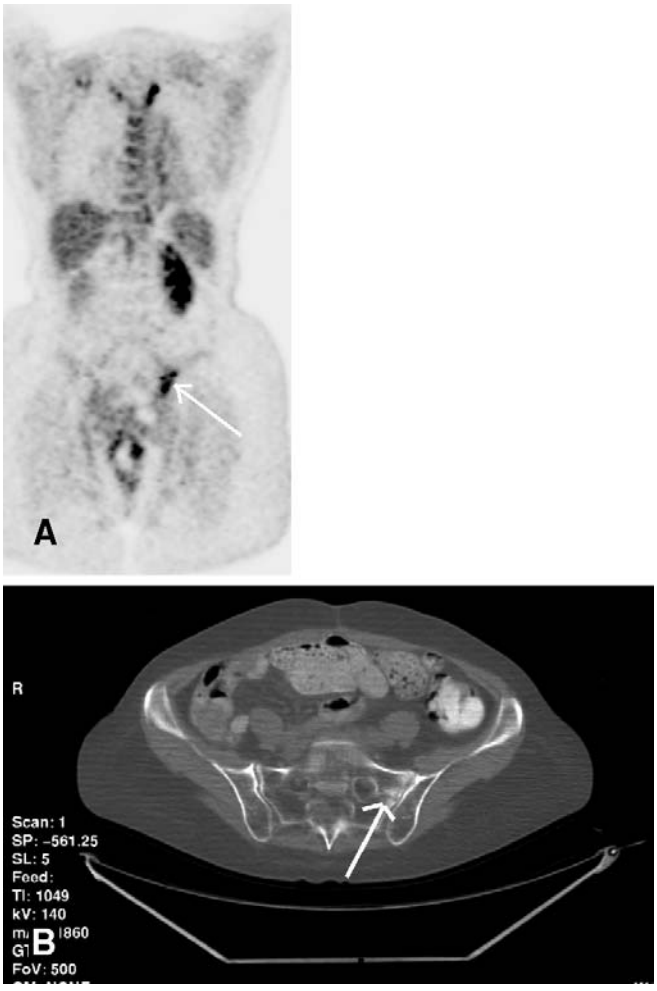

Fig. 6A, B A 73-year-old woman with a history of adenocarcinoma of the rectum who underwent abdominal perineal resection with adjuvant chemotherapy and radiation treatment. Imaging was performed for the evaluation of metastatic disease. **A** PET scan, axial section, shows moderate linear FDG uptake in the left sacrum (*arrow*). **B** CT scan, axial image, shows a left sacral insufficiency fracture (*arrow*)

tion. The strengths and weakness of CT, MRI, PET and bone scan are discussed below.

Computed tomography

The role of CT in the diagnosis of stress fractures is well established. The typical appearance of a stress fracture by CT is that of focal callus formation and endosteal thickening around a fracture site [15, 22, 23, 24, 25, 26, 27]. Occasional increased medullary cavity density and adjacent soft tissue swelling is identified, but there is overlap in these latter features with pathologic fractures [22, 28]. Helpful signs for distinguishing stress fractures from pathologic fractures are the presence of an aggressive periosteal reaction or bone marrow pattern of destruction. Also, the presence of endosteal scalloping, mineralized matrix and a large soft tissue mass, are often exquisitely defined by CT. Intravenous contrast is not required, although nodular and mass-like areas of enhancement may affirm the presence of an underlying mass [29]. It should be noted that viable tumor, reactive hyperemia and inflammatory tissue will all demonstrate contrast enhancement, although dynamic post-contrast imaging may play a role in distinguishing malignant from non-malignant tissue [30].

In a series reported by Somer in 1982, a visible fracture line was only seen in one of 12 cases of stress fractures [23]. The inability of CT to portray the fracture lines is probably in part explained by the evolution in CT technology between 1982 and the present day. With the advent of 16-slice MDCT, isotropic data sets and three-dimensional (3D) imaging, bone detail may be further enhanced to more easily detect the fracture lines of a stress fracture. Furthermore, subtle destruction of the cortex and bone marrow in a pathologic fracture will permit the detection of the underlying bone marrow lesion. The utility of 3D CT imaging cannot be overemphasized in the evaluation of skeletal pathology, as multiplanar reformatted 3D CT images have been shown to alter treatment decisions in up to 30% of cases [31] and display additional pathology in up to 50% of cases [32]. With regard to stress fractures, a fracture line in the axial plane may be easily overlooked by conventional axial CT but well demonstrated by coronal or sagittal multiplanar or volume rendered 3D CT (Fig. 1). In the assessment of pathologic fractures, 3D CT images are essential for defining the longitudinal boundaries and morphology of the underlying lesions (Fig. 7).

Magnetic resonance imaging

Unlike radiographs and CT, MRI indisputably depicts abnormalities in the bone marrow [25, 33, 34] and is better suited to distinguishing stress fractures from pathologic fractures [19] (Fig. 8). MRI findings in a stress fracture are discernible before radiographic abnormalities and features include decreased marrow signal on T1-weighted imaging and increased marrow signal on T2-weighted imaging around a fracture line [25, 35, 36, 37, 38, 39]. Such signal changes in the bone marrow sound to be rather nonspecific. In stress fractures, T2 signal changes suggest edema [38, 40]; in pathologic fractures, T2 signal changes may represent a mixture of tumor and edema. How, then, is an underlying lesion distinguished by MRI? The assessment of T1 signal changes is in fact fundamental to the detection of a pathologic fracture. In our experience with long bone fractures, the most sensitive discriminating feature between stress and pathologic fractures is that of a well-defined low signal T1-weighted

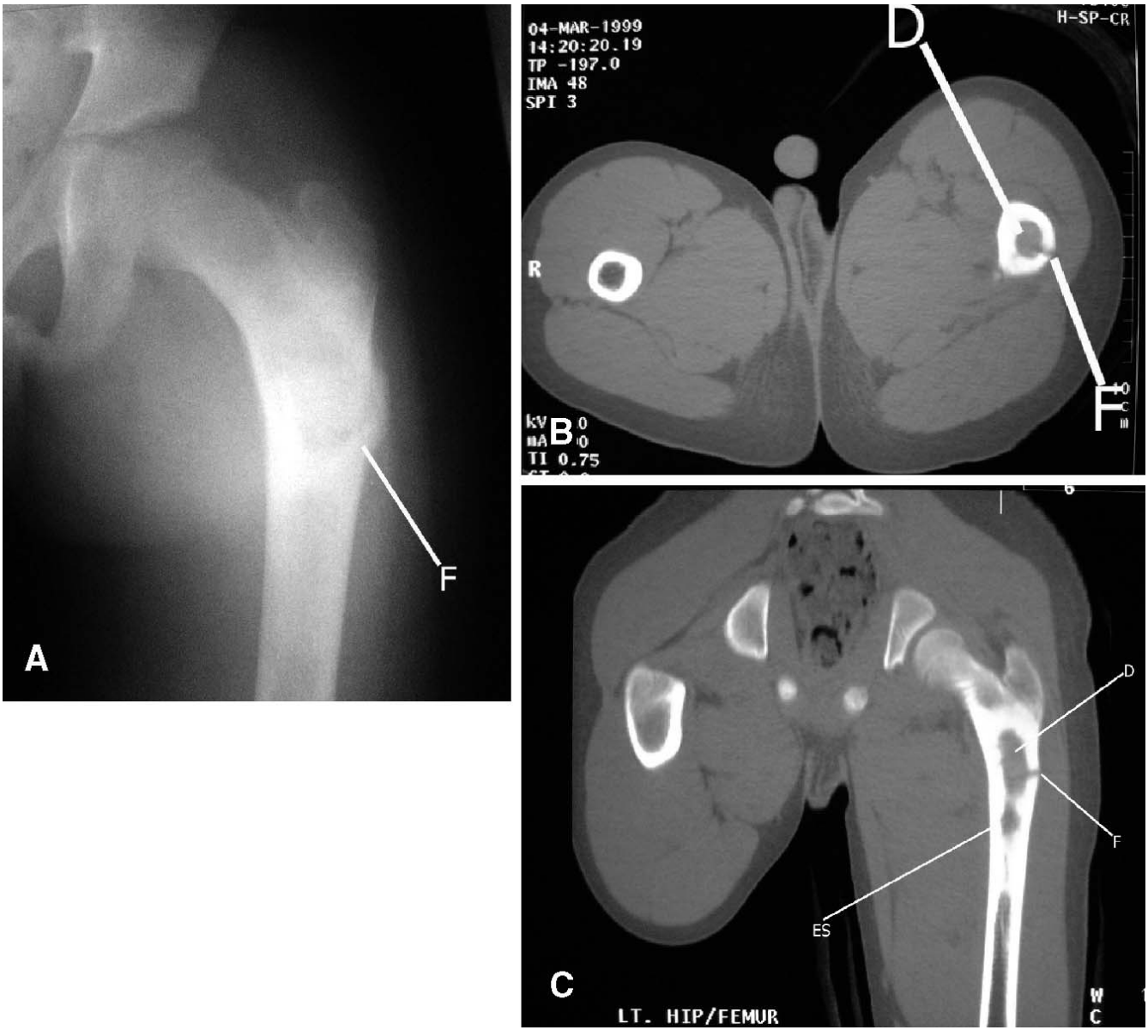

Fig. 7A—C A 10-year-old boy who fell down the stairs. Radiography revealed a fracture. An underlying lesion was suspected. CT depicted the underlying lesion with certainty and biopsy revealed fibrous dysplasia. **A** Radiograph of the femur shows a fracture (*F*). **B** Axial CT image shows a left femoral fracture (*F*) and increased density (*D*) in the medullary canal compared with the right femur. Increased density around a fracture is a nonspecific finding that may be seen with stress fractures as well. **C** Coronal reformatted CT image shows the fracture (*F*); an underlying lesion is obvious given endosteal scalloping (*ES*) and the ground-glass density (*D*) of fibrous dysplasia

abnormality around a fracture indicating an underlying tumor. T2 signal changes are not as specific. Such findings are echoed in a report by Yuh indicating that complete replacement of fatty marrow signal within a vertebral body on T1-weighted imaging is a distinguishing characteristic of malignant vertebral fractures compared with benign fractures [20]. For optimal evaluation of the bone marrow, it should be noted that T1-weighted images need to be performed with a TR under 500 ms. MRI is undoubtedly superior to CT for the detection of an underlying bone marrow lesion.

Advanced MRI techniques have been developed that have been studied in a limited fashion but may prove in the future to assist with distinguishing stress fractures from pathologic fractures. These include chemical shift imaging [41, 42], diffusion weighted imaging [40, 43, 44], dynamic contrast-enhanced imaging [30] and MR spectroscopy [45]. Chemical shift imaging is based on the

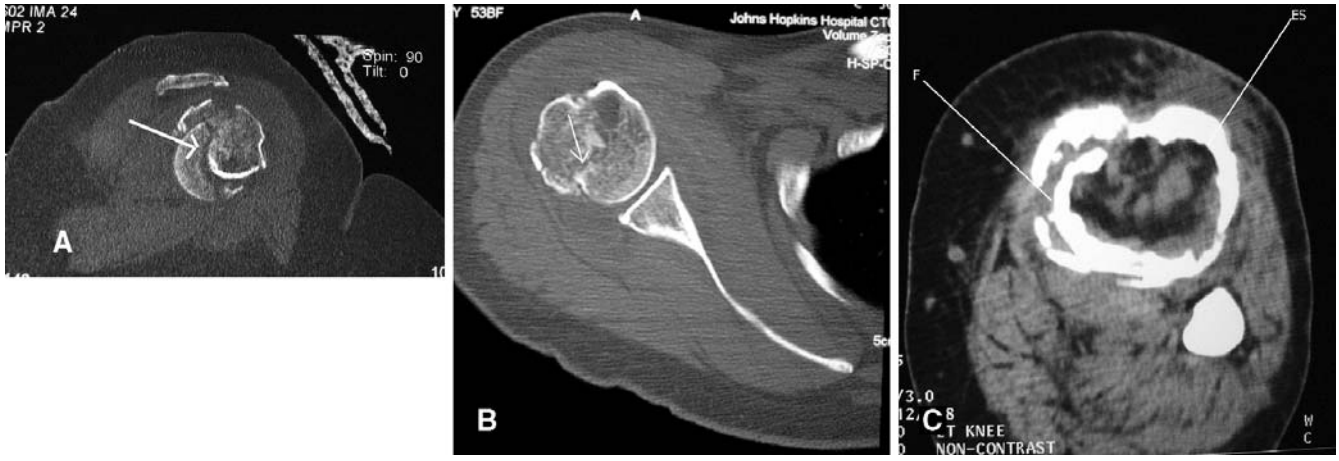

Fig. 8A—C CT depiction of three patients with comminuted fractures. Occasionally, it is difficult to distinguish a stress fracture from a pathologic fracture by CT. Furthermore, benign and malignant pathologic lesions may also be confused. Patient A has a comminuted fracture of the greater tuberosity without an underlying lesion. Patient B has a comminuted pathologic fracture through metastatic breast carcinoma. Patient C has a comminuted fracture through a unicameral bone cyst. **A** Sagittal oblique reformatted CT image in patient A shows the comminuted fracture. Note the intact fracture surface (*arrow*). **B** Axial CT image in patient B shows a comminuted fracture of the greater tuberosity. The underlying lesion is subtle by CT. Note the irregular fracture surface (*arrow*) and surrounding mixed density in the medullary canal. A biopsy revealed metastatic adenocarcinoma. **C** Axial CT image in patient C with a unicameral bone cyst shows a comminuted fracture of the tibia. Note a fallen fragment (*F*), endosteal scalloping (*ES*) and mixed density within the medullary canal

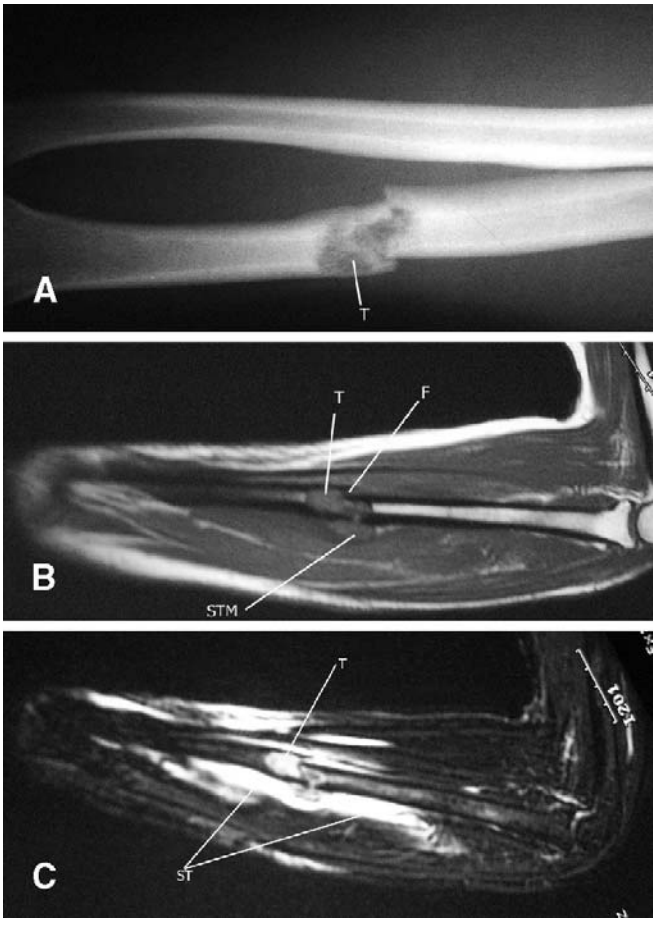

Fig. 9A—C A 53-year-old woman with chronic shoulder pain who heard a popping sound after lifting heavy boxes. A pathologic fracture of the radius was discovered by imaging. Subsequent biopsy revealed a chondrosarcoma and the patient underwent amputation. **A** Radiograph of the forearm shows a pathologic fracture of the radius. An underlying lytic lesion (*T*) is present. **B** Sagittal T1-weighted MR image (SE; TR 440, TE 14) demarcates the well-defined tumor (*T*) around the fracture site (*F*). A small soft tissue mass (*STM*) is also present. **C** Sagittal T2-weighted MR image (FSE; TR 5000, TE 70) shows increased bone marrow signal about the fracture site corresponding to the cartilaginous tumor (*T*). Note the surrounding increased soft tissue signal (*ST*)

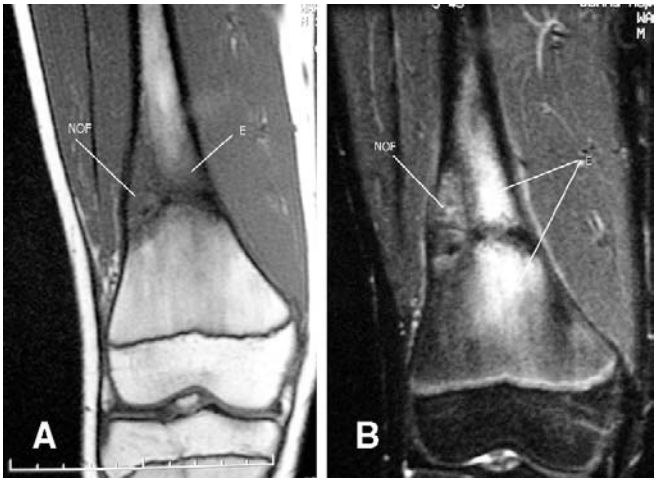

Fig. 10A, B A 14-year-old boy with a history of trauma to the right knee who presented with a fracture through an incidental non-ossifying fibroma (NOF) discovered by radiography. The patient was placed in a cast for 8 weeks and then electively underwent curettage and bone graft. MRI illustrates typical signal changes about the fracture. **A** Coronal T1-weighted MR image (SE; TR 300, TE 9) shows an oblique fracture through an eccentric well-demarcated lesion (*NOF*). Fracture is complete. Note the ill-defined edema (*E*) around the remaining fracture line. **B** Corresponding coronal inversion recovery sequence (FSEIR; TR 4000, TE 30, TI 160) again shows the lesion (*NOF*) and edema (*E*)

principle that a voxel which contains both water and fatty marrow elements, as present in a stress fracture, should demonstrate a drop in signal on an opposed-phase gradient echo sequence compared with an in-phase gradient echo sequence (Fig. 13). However, in a voxel in which normal marrow elements are completely replaced by tumor (the case of a pathologic fracture), there is no drop in signal expected on the opposed-phase sequence compared with the in-phase sequence. Diffusion weighted imaging has been successfully used in the assessment of vertebral fractures and is the only noninvasive technique that maps the motion of water protons [43, 44]. In the case of a pathologic fracture, there is restriction of water motion at the site of tumor whereas in a stress fracture, mobility of the water protons is preserved. In this way, stress fractures may be differentiated from pathologic fractures.

Other cross-sectional features that aid in distinguishing between stress fractures and pathologic fractures are common to both CT and MRI, and include the presence of a soft tissue mass and endosteal scalloping, but periosteal and cortical signal changes are nonspecific. The character of a periosteal reaction is not as discernible by MRI as it is by CT.

On the other hand, muscle signal abnormalities are much more clearly identified by MRI than CT. Hanna et al. described that massive edema in the muscles surrounding a bone tumor was an ominous clinical finding, more commonly found in malignant rather than benign underlying lesions and typically involved the disruption of a muscle attachment to bone by the tumor [46]. Hence, muscle signal changes around a pathologic fracture may represent edema rather than tumor infiltration in many cases.

Whole body imaging: positron emission tomography, bone scan and MRI

Finally, for a whole-body approach, bone scans and PET scans carry a distinct advantage over CT and MRI, but they are nonspecific. In the evaluation of stress injuries, a bone scan can reveal changes before radiography but there is nonspecific activity at the site of fracture (Fig. 11) [9, 10]. Bone scans are lacking in resolution and specificity to differentiate stress and pathologic fractures. Similarly, PET scans may show FDG uptake at the site of a stress fracture, potentially mistaking the presence of a metastatic focus (Fig. 5) [11]. However, with the introduction of PET-CT scanners, interpretation of a PET scan in conjunction with CT features is easily achieved and critical for precise diagnosis. ^{18}F-FDG accumulation has been described in the setting of benign fractures of the ribs, clavicle and sacrum [7, 8, 11] and knowledge and recognition of this important and potential pitfall of PET can prevent inappropriate treatment and avoid unnecessary bone biopsy.

Whole body MRI screening is a recent addition to the arsenal of techniques available for evaluation of diffuse bone metastases and rivals bone scan [47]. Thus, for the assessment of a particular fracture site as well as a complete screen for bone metastases, MRI may offer the most comprehensive approach to the assessment of a patient with a fracture and potentially multiple lesions.

Conclusion

Accurate radiologic differentiation of a stress fracture from a pathologic fracture is paramount. The recognition of sensitive radiologic features for differentiating the two entities will guide appropriate therapy in the case of a pathologic fracture and avoid inappropriate treatment of a stress fracture. A suggested algorithm for investigating fractures is shown in Fig. 14.

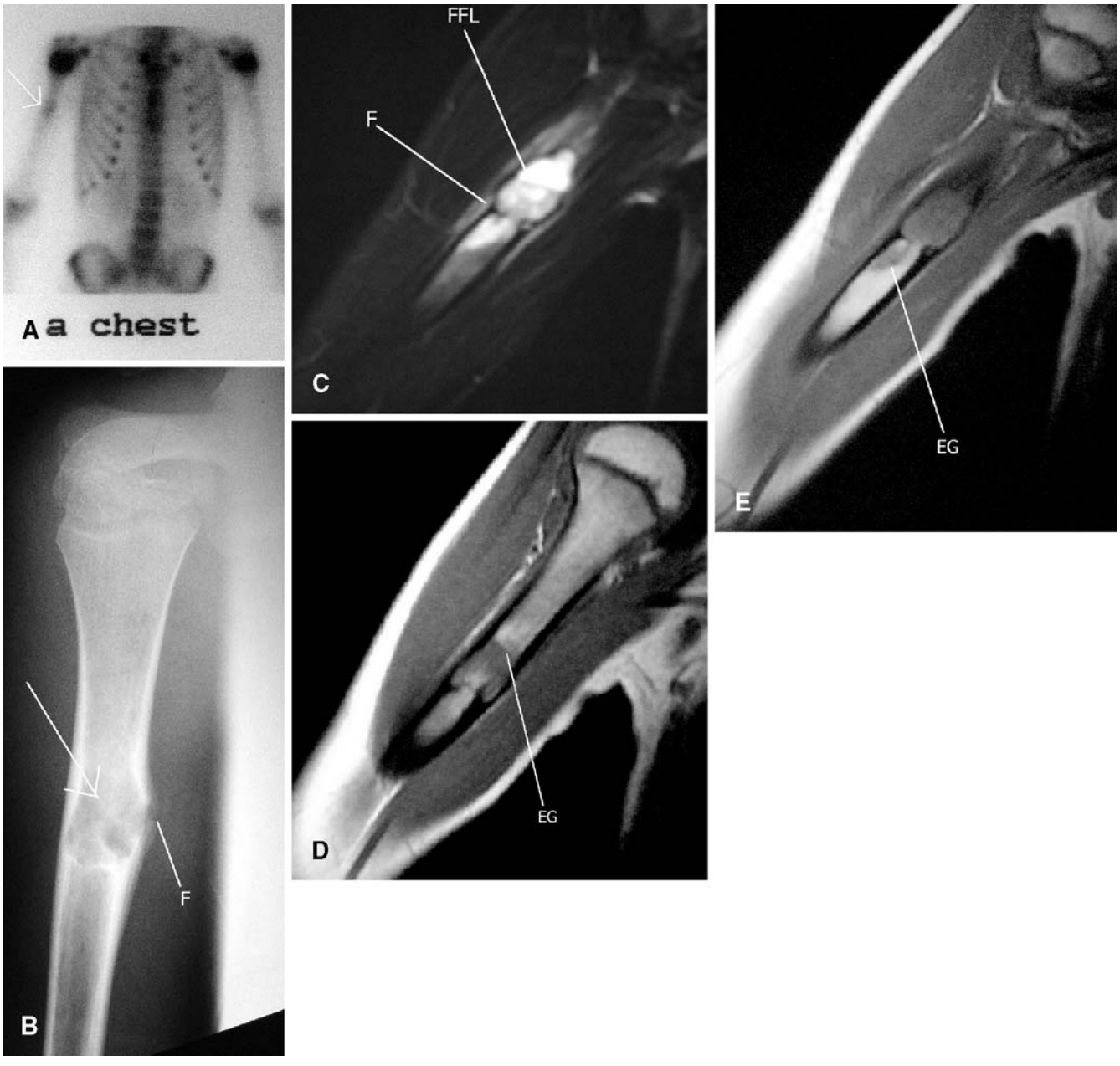

Fig. 11A—E An 8-year-old girl with pain in the humerus. Investigation revealed a pathologic fracture of eosinophilic granuloma (EG). **A** Bone scan showing focal increased uptake in the midhumerus (*arrow*). **B** Radiograph of the humerus showing a subtle fracture (*F*) traversing a lytic lesion in the humerus (*arrow*). **C** Coronal T2-weighted MR image (FSE; 5000, 80) shows a well-defined lesion containing fluid-fluid levels (*FFL*) associated with a fracture (*F*). Fluid-fluid levels may be present in any lesion with a fracture. They are not specific for a particular entity in the setting of a pathologic fracture. **D** Coronal T1-weighted MR image (SE; 700, 13) shows a well-defined superior border of the lesion (*EG*). **E** Coronal T1-weighted MR image (SE; 700, 13) obtained more posteriorly shows a well-defined inferior border of the lesion (*EG*)

Fig. 12A—H A 28-year-old woman with a history of chronic knee pain. Radiographs and MR images of the knee revealed no significant abnormalities. The symptoms persisted and subsequent bone scan demonstrated nonspecific increased uptake along the mid-femoral diaphysis. CT and MR images of the femur are shown. Biopsy revealed malignant fibrous histiocytoma. **A** Bone scan reveals increased uptake in the femur (*arrows*) around a linear photopenic area (*F*). **B** Radiograph of the femur shows a pathologic fracture. A permeative pattern of destruction is present (*arrows*). **C** Axial contrast-enhanced CT image at the level of the fracture (*F*) shows a soft tissue mass (*M*) and cortical destruction (*arrow*). **D** Axial contrast-enhanced CT image superior to the level of the fracture shows the cortical destruction in more detail (*arrows*). **E** Coronal T1-weighted MR image (SE; TR 400, TE 14) shows a well-defined bone marrow signal abnormality (*BM*) representing the underlying mass in the femur and surrounding soft tissue mass (*STM*). **F** Coronal T2-weighted MR image (FSE; TR 5000, TE 90) shows the fracture line (*F*) to best advantage with the surrounding bone marrow (*BM*) and soft tissue mass (*STM*). **G** Axial T1-weighted MR image (SE; TR 400, TE 14) again shows decreased signal in the bone marrow (*BM*), endosteal scalloping (*ES*) and the soft tissue mass (*STM*). **H** Axial contrast-enhanced T1-weighted MR image (FSPGR; TR 220, TE 4.2, flip angle 70°) shows nodular enhancement of the mass within the bone marrow (*BM*) as well as enhancement of the soft tissue component (*STM*)

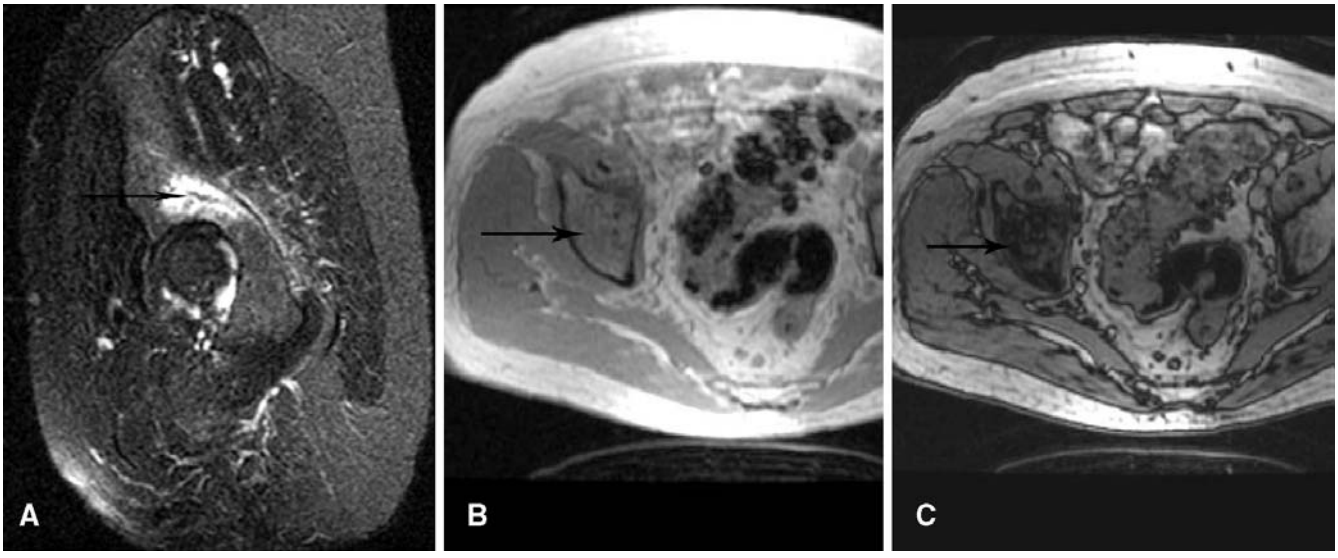

Fig. 13A—C A 54-year-old man with a history of colon cancer and hip pain. **A** Sagittal fat-suppressed T2-weighted MR image (FSE; 4800, 78) shows a fracture (*arrow*) with surrounding bone marrow abnormality in the acetabulum. **B** Axial T1-weighted in-phase MR image (GRE; 225, 4.4) shows subtle signal abnormality in the acetabulum (*arrow*). **C** Axial T1-weighted opposed-phase MR image (GRE; 225, 2.2) shows a drop in bone marrow signal of approximately 50% within the acetabulum surrounding the fracture site, compared with the in-phase image (*arrow*). The drop in signal is seen in voxels which contain edema interspersed with fatty marrow elements, a finding that is expected in stress fractures; no drop in signal is expected around pathologic fractures since fatty marrow elements are replaced by tumor. This patient had an acetabular stress fracture

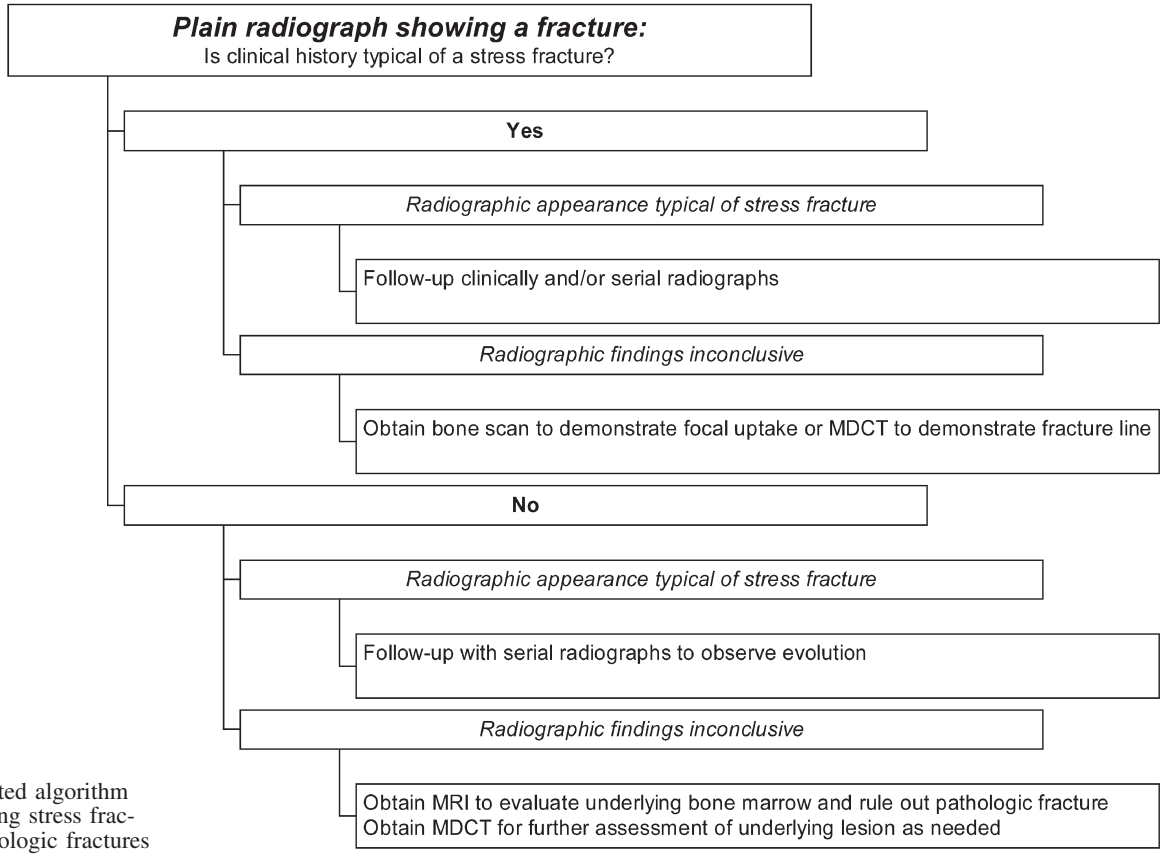

Fig. 14 Suggested algorithm for differentiating stress fractures from pathologic fractures

References

1. Pentecost RL, Murray RA, Brindley HH. Fatigue, insufficiency, and pathologic fractures. JAMA 1964;187:1001–1004.
2. Blatz DJ. Bilateral femoral and tibial shaft stress fractures in a runner. Am J Sports Med 1981; 9:322–325.
3. Orava S, Jormakka E, Hulkko A. Stress fractures in young athletes. Arch Orthop Trauma Surg 1981; 98:271–274.
4. Korpelainen R, Orava S, Karpakka J, Siira P, Hulkko A. Risk factors for recurrent stress fractures in athletes. Am J Sports Med 2000; 29:304–310.
5. Schickendantz MS, Ho CP, Koh J. Stress injury of the proximal ulna in professional baseball players. Am J Sports Med 2002; 30:737–741.
6. Hulkko A, Orava S. Stress fractures in athletes. Int J Sports Med 1987; 8:221–226.
7. Shon IH, Fogelman I. F-18 FDG positron emission tomography and benign fractures. Clin Nucl Med 2003; 28:171–175.
8. Meyer M, Gast T, Raja S, Hubner K. Increased F-18 accumulation in an acute fracture. Clin Nucl Med 1994; 19:13–14.
9. Wilcox JR, Moniot AL, Green P. Bone scanning in the evaluation of exercise related stress injuries. Radiology 1977; 123:699–703.
10. Deutsch AL, Coel MN, Mink JH. Imaging of stress injuries to bone. Radiography, scintigraphy, and MR imaging. Clin Sports Med 1997;16:275–290.
11. Fayad LM, Cohade C, Wahl RL, Fishman EK. Sacral fractures: a potential pitfall of FDG positron emission tomography. AJR Am J Roentgenol 2003; 181:1239–1243.
12. Soubrier M, Dubost JJ, Boisgard S, Sauvezie B, Gaillard P, Michel JL, Ristori JM. Insufficiency fracture. A survey of 60 cases and review of the literature. Joint Bone Spine 2003; 70:209–218.
13. Anderson MW, Ugalde V, Batt M, Gacayan J. Shin splints: MR appearance in a preliminary study. Radiology 1997; 204:177–180.
14. Umans HR, Kaye JJ. Longitudinal stress fractures of the tibia: diagnosis by magnetic resonance imaging. Skeletal Radiol 1996; 25:319–324.
15. Allen GJ. Longitudinal stress fractures of the tibia: diagnosis with CT. Radiology 1988; 167:799–801.
16. Resnick D, Goergen TG, Pathria MN. Physical Injury. In: Resnick, D, ed. Bone and joint imaging, 2nd edn. Philadelphia: WB Saunders, 1996:723–815.
17. Buckwalter JA, Brandser EA. Stress and insufficiency fractures. Am Fam Physician 1997; 56:175–182.
18. Shearman CM, Brandser EA, Parman LM, et al. Longitudinal tibial stress fractures: a report of eight cases and review of the literature. J Comput Assist Tomogr 1998; 22:265–269.
19. Pauleit D, Sommer T, Textor J, et al. MRI diagnosis in longitudinal stress fractures: differential diagnosis of Ewing sarcoma. Rofo Fortschr Geb Rontgenstr Neuen Bildgeb Verfahr 1999; 170:28–34.
20. Yuh WTC, Zachar CK, Barloon TJ, Sato Y, Sickels WJ, Hawes DR. Vertebral compression fractures: distinction between benign and malignant causes with MR imaging. Radiology 1989; 172:215–218.
21. Bertuna G, Fama P, Lo Nigro L, Russo-Mancuso G, Di Cataldo A. Marked osteoporosis and spontaneous vertebral fractures in children: don't forget, it could be leukemia. Med Pediatr Oncol 2003; 41:450–454.
22. Yousem D, Magid D, Fishman EK, Kuhajda F, Siegelman SS. Computed tomography of stress fractures. J Comput Assist Tomogr 1986; 10:92–95.
23. Somer K, Meurman KO. Computed tomography of stress fractures. J Comput Assist Tomogr 1982; 6:109–115.
24. Murcia M, Brennan RE, Edeiken J. Computed tomography of stress fracture. Skeletal Radiol 1982; 8:193–195.
25. Feydy A, Drape JL, Beret E, et al. Longitudinal stress fractures of the tibia: comparative study of CT and MR imaging. Eur Radiol 1998; 8:598–602.
26. Spitz DJ, Newberg AH. Imaging of stress fractures in the athlete. Radiol Clin North Am 2002; 40:313–331.
27. Lingg GM, Soltesz I, Kessler S, Dreher R. Insufficiency and stress fractures of the long bones occurring in patients with rheumatoid arthritis and other inflammatory diseases, with a contribution on the possibilities of computed tomography. Eur J Radiol 1997; 26:54–63.
28. Reinus WR, Gilula LA, Donaldson S, Shuster J, Glicksman A, Vietti TJ. Prognostic features of Ewing sarcoma on plain radiograph and computed tomography scan after initial treatment. A Pediatric Oncology Group study (8346). Cancer 1993; 72:2503–2510.
29. Murphey MD, wan Jaovisidha S, Temple HT, Gannon FH, Jelinek JS, Malawer MM. Telangiectatic osteosarcoma: radiologic-pathologic comparison. Radiology 2003; 229:545–553.
30. van der Woude HJ, Bloem JL, Verstraete KL, Taminiau AH, Nooy MA, Hogendoorn PC. Osteosarcoma and Ewing's sarcoma after neoadjuvant chemotherapy: value of dynamic MR imaging in detecting viable tumor before surgery. AJR Am J Roentgenol 1995; 165:593–598.
31. Scott WW Jr, Fishman EK, Magid D. Acetabular fractures: optimal imaging. Radiology 1987; 165:537–539.
32. Newton PO, Hahn GW, Fricka KB, Wenger DR. Utility of three-dimensional and multiplanar reformatted computed tomography for evaluation of pediatric congenital spinal anomalies. Spine 2002; 27:844–850.
33. Soderlund V, Radiological diagnosis of skeletal metastases. Eur Radiol 1996; 6:587–595.
34. Mirzaei S, Filipits M, Keck A, Bergmayer W, Knoll P, Koehn H, Ludwig Pecherstorfer M. Comparison of Technetium-99m MIBI imaging with MRI for detection of spine involvement in patients with multiple myeloma. BMC Nucl Med 2003; 3:2.
35. Stafford SA, Rosenthal DI, Gebhardt MC, Brady TJ, Scott JA. MRI in stress fracture. AJR Am J Roentgenol 1986; 147:553–556.
36. Tyrrell PNM, Davies AM. Magnetic resonance imaging appearances of fatigue fractures of the long bones of the lower limb. Br J Radiol 1994; 67:332–338.
37. Cabitza P, Tamim H. Occult fractures of tibial plateau detected employing magnetic resonance imaging. Arch Orthop Trauma Surg 2000; 120:355–357.
38. Yamamoto T, Schneider R, Bullough PG. Subchondral insufficiency fracture of the femoral head: histopathologic correlation with MRI. Skeletal Radiol 2001; 30:247–254.
39. Lee JK, Yao L. Stress fractures: MR imaging. Radiology 1988; 169:217–220.
40. Baur A, Stabler A, Arbogast S, Duerr HR, Bartl R, Reiser M. Acute osteoporotic and neoplastic vertebral compression fractures: fluid sign at MR imaging. Radiology 2002; 225:730–735.
41. Zampa V, Cosottini M, Michelassi C, Ortori S, Bruschini L, Bartolozzi C. Value of opposed-phase gradient-echo technique in distinguishing between benign and malignant vertebral lesions. Eur Radiol 2002; 12:1811–1818.
42. Disler DG, McCauley TR, Ratner LM, Kesack CD, Cooper JA. In-phase and out-of-phase MR imaging of bone marrow: prediction of neoplasia based on the detection of coexistent fat and water. AJR Am J Roentgenol 1997; 169:1439–1447.

43. Spuentrup E, Buecker A, Adam G, van Vaals JJ, Guenther RW. Diffusion-weighted MR imaging for differentiation of benign fracture edema and tumor infiltration of the vertebral body. AJR Am J Roentgenol 2001; 176:351–358.
44. Herneth AM, Phillip MO, Naude J, Funovics M, Beichel RR, Bammer R, Imhof H. Vertebral metastases: assessment with apparent diffusion coefficient. Radiology 2002; 225:889–894.
45. Oya N, Aoki J, Shinozaki T, Watanabe H, Takagishi K, Endo K. Preliminary study of proton magnetic resonance spectroscopy in bone and soft tissue tumors: an unassigned signal at 2.0–2.1 ppm may be a possible indicator of malignant neuroectodermal tumor. Radiat Med 20000; 18:193–198.
46. Hanna SL, Fletcher BD, Parham DM, Bugg MF. Muscle edema in musculoskeletal tumors: MR imaging characteristics and clinical significance. J Magn Reson Imaging 1991; 1:441–449.
47. Steinborn M, Heuck AF, Tiling R, Bruegel M, Gauger L, Reiser MF. Whole-body bone marrow MRI in patients with metastatic disease to the skeletal system. J Comput Assist Tomogr 1999; 23:123–129.